iScience

CellPress
OPEN ACCESS

Article

The contact force between lunar-based equipment and lunar soil

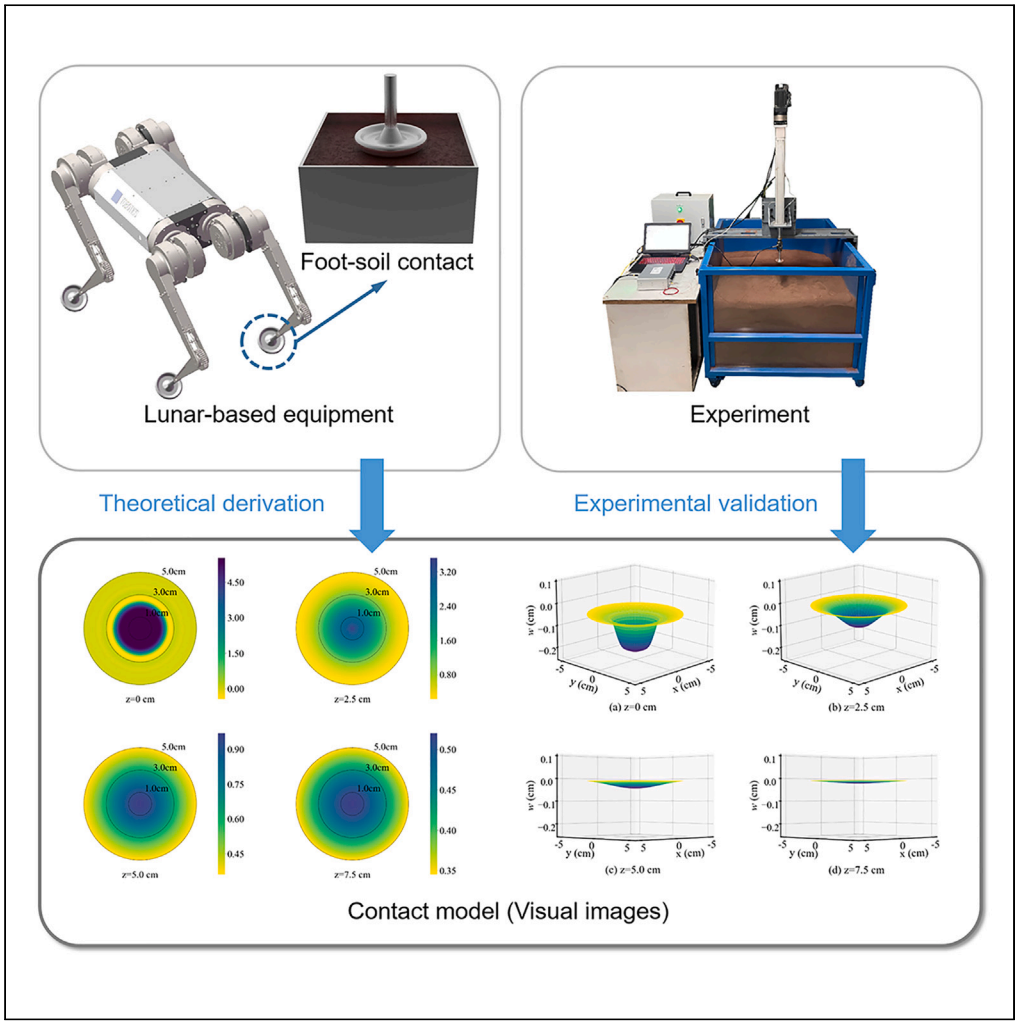

Zheng-Han Chen, Zhao-Dong Xu, Hong-Fang Lu, ..., Bo Pan, Xue-Liang Zhao, Zhong-Wei Hu

zhdxu@163.com

Highlights

Theoretical model reveals the vertical contact mechanism between foot and lunar soil

Theoretical results are depicted using visual images

Proposed model is validated through experiment

Accuracy in lunar environment is validated through simulation

Chen et al., iScience *27*, 109322
April 19, 2024
https://doi.org/10.1016/j.isci.2024.109322

iScience

CellPress
OPEN ACCESS

Article

The contact force between lunar-based equipment and lunar soil

Zheng-Han Chen,[1] Zhao-Dong Xu,[2,9,*] Hong-Fang Lu,[3] Deng-Yun Yu,[4] Jian-Zhong Yang,[5] Bo Pan,[6] Xue-Liang Zhao,[7] and Zhong-Wei Hu[8]

SUMMARY

Lunar-based equipment plays a vital role in the exploration of the moon because it undertakes the tasks of moving, transporting, digging, and so on. In order to control the gait of lunar-based equipment more precisely and guarantee mobile stability, the contact mechanism between its foot and lunar soil is worthy of in-depth study. In this paper, a contact model is proposed to predict the stress, strain, and displacement both on the contact surface and in the lunar soil when the foot is under vertical load. The axial stress in the proposed contact model is verified through the experiment and its accuracy in the lunar equipment is verified through simulation. The error is in a reasonable range and the influence depth of load conforms to the experiment results. This paper provides a relatively accurate model to describe the contact force between the lunar-based equipment's foot and the lunar soil and will promote the research of lunar exploration.

INTRODUCTION

The discovery of the moon was the first step of deep space exploration and it was the dream of mankind for thousands of years. Since the middle of the 20th century, many countries and institutions proposed lunar exploration projects, such as the Apollo Program of the USA, the Infiltrator Program of Russia, the Artemis Program of Japan, the SMART-1 Program of ESA, and so on.[1–3] Some projects have achieved plenty of results and thus encourage scholars to conduct more relative research. In recent years, several countries with aerospace foundations have proposed plans to build unmanned scientific research stations on the moon. There is no doubt that lunar exploration has important scientific value and strategic significance.

The lunar-based equipment plays an important role in the exploration of the moon.[4–6] Lunar-based equipment is a general name for legged robots, wheeled robots, landers, and other special equipment applied on the lunar surface. The equipment discussed in this paper is legged robots. Although wheeled robots have a stable movement performance, legged robots have a better ability to adapt to the environment.[7–9] Many researchers are committed to the development of legged lunar-based equipment and the application on the moon.[10–14]

In existing dynamics studies of legged lunar-based equipment, the object often focuses on the overall performance of lunar-based equipment during the landing or walking process, such as possibility of tipping or damage.[15–19] The vast majority of such studies are based on simulations of the overall dynamics process. However, such simulation studies lack the ability to provide a deep theoretical explanation of the interaction process between lunar soil and lunar-based equipment. Actually, this is a crucial detail that fundamentally determines the safety of the entire lunar-based equipment. Some detailed scientific issues are awaiting further investigation. For example, the distribution of the surface pressure on the different parts of the contact surface is not clear; meanwhile, how the surface pressure is transmitted into the lunar soil is also not clear. Besides, the sinkage depth of feet, which is closely related to the stability of lunar-based equipment, is also not sufficiently clear in the existing literature. Therefore, there is a need for a theoretical model to describe the stress and sinkage of the contact surface, providing a clearer understanding of the contact mechanics between the foot and lunar soil.

Although most of the existing research investigates the above issues from an experimental or simulation perspective, there are still some scholars who have conducted theoretical research on the above issues in the last few decades.[20,21] Existing research on foot-soil contact mechanism can be divided into two main categories: theories based on Bekker-Janosi model and theories based on Terzaghi model. For Bekker-Janosi theories, there is already some outstanding research explaining the contact mechanisms.[22,23] Nevertheless, this kind of theories is highly dependent on the parameters that are difficult to determine when the research subject is lunar soil.[24] The calibration of these

[1]China-Pakistan Belt and Road Joint Laboratory on Smart Disaster Prevention of Major Infrastructures, Southeast University, Nanjing 210096, China
[2]China-Pakistan Belt and Road Joint Laboratory on Smart Disaster Prevention of Major Infrastructures, Southeast University, Nanjing 210096, China
[3]China-Pakistan Belt and Road Joint Laboratory on Smart Disaster Prevention of Major Infrastructures, Southeast University, Nanjing 210096, China
[4]China Aerospace Science and Technology Corporation, Beijing 100048, China
[5]China Aerospace Science and Technology Corporation, Beijing 100048, China
[6]China Aerospace Science and Technology Corporation, Beijing 100048, China
[7]China-Pakistan Belt and Road Joint Laboratory on Smart Disaster Prevention of Major Infrastructures, Southeast University, Nanjing 210096, China
[8]China-Pakistan Belt and Road Joint Laboratory on Smart Disaster Prevention of Major Infrastructures, Southeast University, Nanjing 210096, China
[9]Lead contact
*Correspondence: zhdxu@163.com
https://doi.org/10.1016/j.isci.2024.109322

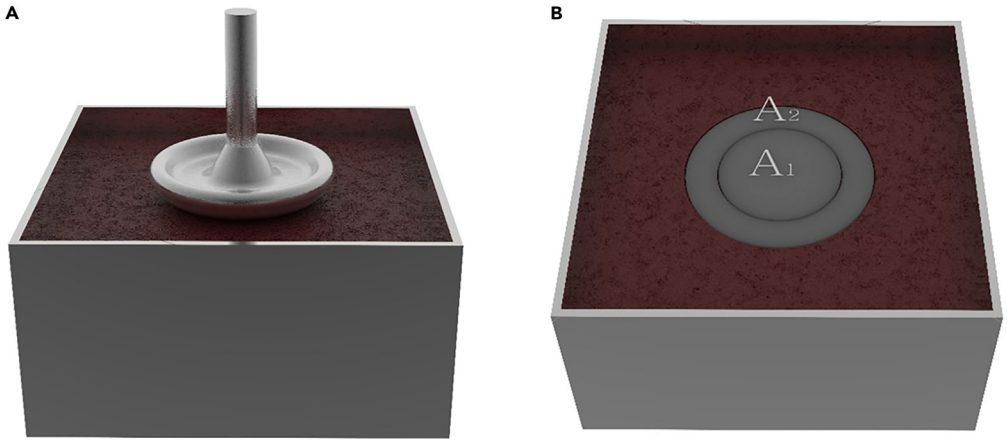

Figure 1. Diagram of the vertical contact
(A) Vertical contact.
(B) Contact area.

parameters often requires a significant amount of effort and relies on experimental groundwork, thus the accuracy in lunar soil is yet to be verified. For Terzaghi theories, this kind of theories originates from the calculation of stress in building foundations.[25,26] This method only focuses on the ultimate bearing capacity of the ground and does not explain the dynamic processes.[27,28] Meanwhile, it is hard to analyze the stress distribution at different positions of the bottom as well as other detailed mechanical performances.[29,30]

As discussed, an important challenge in dynamics analysis on lunar-based equipment is the accurate contact mechanism between the foot and lunar soil, which relates to the impact of lunar soil on the entire lunar-based equipment. The main innovation in this study is to propose an accurate contact model to reveal the vertical contact mechanism between the foot of lunar-based equipment and lunar soil. Some important mechanical performances are accurately calculated, such as surface pressure, stress, and displacement. Meanwhile, the depth and extent of the development of contact force into the lunar soil are also discussed. The accuracy of the proposed contact model is validated by the terrestrial experiment, and the adaptability to the lunar environment with low-gravity and high-vacuum has been validated through simulation.

RESULTS

The exploration of the moon relies on the lunar-based equipment and the equipment which takes the form of legged robots. To investigate the impact of lunar soil on the foot and upper structure, the contact force between the foot and the lunar soil as well as the stress and displacement of the lunar soil is necessary to be studied. In this paper, a contact model is proposed to predict the stress, strain, and displacement both on the contact surface and in the lunar soil. The model is derived theoretically through Hankel integral transformation and takes the mechanical properties of lunar soil into consideration. Afterward, visual images of the theoretical solutions are drawn to illustrate more clearly. The contact experiment is carried out and the axial stress is selected as a representative to verify the proposed contact model. The experimental results are compared with the theoretical ones and the error is within a reasonable range. Moreover, the accuracy of the proposed model in the lunar equipment is validated through simulation. To sum up, the contact model proposed in this paper is proved to be correct. This model can be further used in the research of gait planning and stability analysis of lunar-based equipment to promote the development of lunar exploration.

Conditions of foot-lunar soil contact

When the lunar-based equipment is on a mission such as jumping or walking on the lunar surface, its feet installed at the end of mechanical legs are in direct contact with the lunar soil. In many scenarios, the foot has a vertical load on the lunar surface, as shown in Figure 1A. The foot of the lunar-based equipment has the upper and lower surface with round shapes, and the transition between them is arcuated. The area in which the lunar soil is in contact with the lower surface is defined as A_1, and the area connected to the foot's arcuated edge is defined as A_2, as shown in Figure 1B. The pressure of the foot from the lunar-based equipment can be divided into two parts according to the area ratio and acts on the two areas, as described in Equation 1:

$$P_n = P \cdot s_n / (s_1 + s_2), n = 1, 2. \quad \text{(Equation 1)}$$

where P is the total force, P_1 and P_2 are the sum of distributed force on A_1 and A_2, and s_1 and s_2 are the area of A_1 and A_2, respectively.

We define r_1 as the radius of the lower surface and r_2 as the radius of the upper surface. When the entire arcuated edge is in contact with the lunar soil, we have $s_1 = \pi r_1^2$ and $s_2 = \pi(r_2^2 - r_1^2)$. Hence, $P_1 = P \cdot r_1^2/r_2^2$, and $P_2 = P \cdot (1 - r_1^2/r_2^2)$. When the load caused by the equipment is vertical, the force on the lunar surface is symmetrical. In other words, the pressure is distributed symmetrically on A_1 and A_2. For the circular area A_1, the load is uniformly distributed and the actual contact area equals to s_1. For the ring area A_2, the actual contact area equals to the

area of the arcuated contact surface, and it is approximately considered that the load is also uniform. The actual contact area s_{2a} of A_2 is calculated as $s_{2a} = \pi^2 r_2(r_2 - r_1)$. Therefore, the uniformly distributed loads q_1 and q_2 on the two areas can be expressed as:

$$\begin{cases} q_1 = P_1 \Big/ s_1 = \dfrac{P}{\pi} \cdot \dfrac{1}{r_2^2} \\ q_2 = P_2 \Big/ s_{2a} = \dfrac{P}{\pi^2} \cdot \dfrac{r_1 + r_2}{r_2^3} \end{cases} \quad \text{(Equation 2)}$$

Proposed contact model

The stress and displacement components under the vertical load of the lunar-based equipment's foot should be calculated as the sum of three parts: (1) stress or displacement caused by the geostatic lunar soil, (2) stress or displacement caused by the circular load q_1, and (3) stress or displacement caused by the ring load q_2. Meanwhile, the displacement components are composed of that caused only by (2) and (3). To sum up, the final analytical solutions, namely the proposed contact model, are shown in Equation 3.

$$\begin{cases} \sigma_z = \sigma_z^0 + \sigma_{zq_1r_1} + \sigma_{zq_2r_2} - \sigma_{zq_2r_1} \\ w = w_{q_1r_1} + w_{q_2r_2} - w_{q_2r_1} \end{cases} \quad \text{(Equation 3)}$$

where σ_z^0 is the axial stress caused by the geostatic lunar soil, $\sigma_{zq_1r_1}$ is the axial stress under the circular load q_1 with the radius of r_1, $\sigma_{zq_2r_2}$ is the axial stress under the circular load q_2 with the radius of r_2, $\sigma_{zq_2r_1}$ is the axial stress under the circular load q_2 with the radius of r_1. The definitions about the displacement component w are the same.

Taking $\sigma_{zq_1r_1}$ as an example, the expression of axial stress component is:

$$\begin{aligned} \sigma_{zq_1r_1} = -q_1 \Bigg\{ & \sum_{k=0}^{\infty} \left[\frac{(-1)^k}{k!(k+1)!} \left(\frac{1}{2}\right)^{2k+1} \frac{\Gamma(2k+2)}{(z/r_1)^{2k+2}\Gamma(1)} {}_2F_1\left(k+1, k+\frac{3}{2}; 1; -\frac{r^2}{z^2}\right) \right] \\ & + \sum_{k=0}^{\infty} \left[\frac{(-1)^k}{k!(k+1)!} \left(\frac{1}{2}\right)^{2k+1} \frac{\Gamma(2k+3)}{(z/r_1)^{2k+3}\Gamma(1)} {}_2F_1\left(k+\frac{3}{2}, k+2; 1; -\frac{r^2}{z^2}\right) \right] \Bigg\} \end{aligned} \quad \text{(Equation 4)}$$

Meanwhile, the displacement component w can be expressed as:

$$\begin{aligned} w_{q_1r_1} = \frac{1+\mu}{E} q_1 r_1 \Bigg\{ & (2-2\mu) \sum_{k=0}^{\infty} \left[\frac{(-1)^k}{k!(k+1)!} \left(\frac{1}{2}\right)^{2k+1} \frac{\Gamma(2k+2)}{(z/r_1)^{2k+2}\Gamma(1)} {}_2F_1\left(k+1, k+\frac{3}{2}; 1; -\frac{r^2}{z^2}\right) \right] \\ & + \frac{z}{r_1} \sum_{k=0}^{\infty} \left[\frac{(-1)^k}{k!(k+1)!} \left(\frac{1}{2}\right)^{2k+1} \frac{\Gamma(2k+3)}{(z/r_1)^{2k+3}\Gamma(1)} {}_2F_1\left(k+\frac{3}{2}, k+2; 1; -\frac{r^2}{z^2}\right) \right] \Bigg\} \end{aligned} \quad \text{(Equation 5)}$$

Visual images of the proposed contact model

The axial stress σ_z and axial displacement w deserve the greatest attention, for they are related to the sinkage of the lunar-based equipment's foot. According to the calculation results shown in Equations 25–27 and 30, meanwhile considering the expression Equations 32 and 33 which describe the contact surface, the visual images of σ_z and w are drawn. The total force in the case is defined as $P = 100$ N, thus, the loads acting on region A_1 and A_2 are $q_1 = 5.53$ N/cm^2 and $q_2 = 3.23$ N/cm^2, respectively. The axial stress and axial displacement distributions of four sections are specially demonstrated: $z = 0$ cm, $z = 2.5$ cm, $z = 5$ cm and $z = 7.5$ cm. These sections demonstrate how the axial stress σ_z develop on the contact surface and in a certain depth of the lunar soil. The positions of these sections are demonstrated in Figure 2.

The visual images of the theoretical results of σ_z and w are displayed in Figures 3 and 4. In other words, Figures 3 and 4 illustrates the graphical results of the proposed contact model. The values can be obtained from the color bars next to each figure. The diameters of A_1 and A_2 are 2.0cm and 3.0cm respectively, thus besides the vertical cylinder corresponding to A_1 and A_2, the subfigures in Figures 3 and 4 also show the surrounding area.

It can be obtained from Figure 3 that the axial stress σ_z equals the vertical load q_1 and q_2 in the two regions A_1 and A_2 on the contact surface. This is in line with the actual situation, and also proves the accuracy of our derivation. The axial stress σ_z on the section $z = 2.5$ cm attenuates rapidly with the increase of radial distance r, and the speed and degree of attenuation decrease successively on the section $z = 5.0$ cm and $z = 7.5$ cm. In other words, the difference of σ_z between the center and the edge decreases with increasing depth. On the section $z = 7.5$ cm, σ_z has been reduced to about 1/10 of the surface stress, thus it can be considered that the maximum influence range of the load has been reached.

Figure 4 shows the axial displacement w distribution and the same four sections are displayed. Obviously, on the contact surface, the axial displacement exists only within the scope of the vertical load and its very close surroundings. The difference of w between the center and the edge shows the same law as σ_z. That is to say, as the depth increases, the boundary between the forced region and the non-forced region becomes more blurred. The axial displacement w almost disappears in the last subfigure in Figure 4, thus we have the same the conclusion as σ_z that the maximum influence depth of the vertical load is about 7.5cm. Meanwhile, it can be observed by comparing the axial displacement at the edge in the subfigures that w changes slightly with depth and the value of w is very small. Hence, the influence width of the vertical load

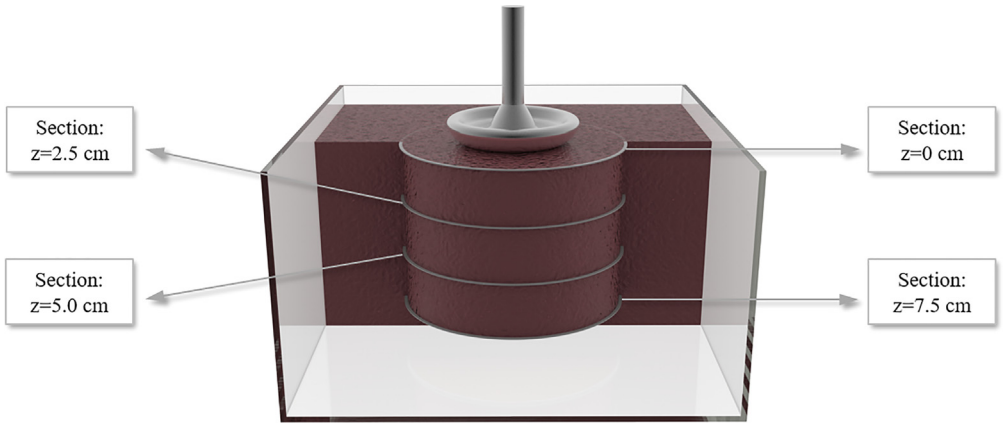

Figure 2. Positions of the sections

is about 5.0cm. To sum up, the influence scope of the vertical contact is a cylinder with the depth of 7.5cm and the radius of 5.0cm in the lunar soil.

In order to see the axial displacement more intuitively, they are displayed in the 3D graph Figure 5. X axis and Y axis represent the horizontal distance to the center of forced region, while z axis represent the axial displacement *w* of each section. What should be noticed is that the proportional scale of z axis is set to be different from the other axes in order to observe the displacement more intuitively. The perspective of Figures 5C and 5D is adjusted to be horizontal to see the difference of height. It can be seen that the absolute value of *w* is too small to be observed on the section z = 7.5 cm.

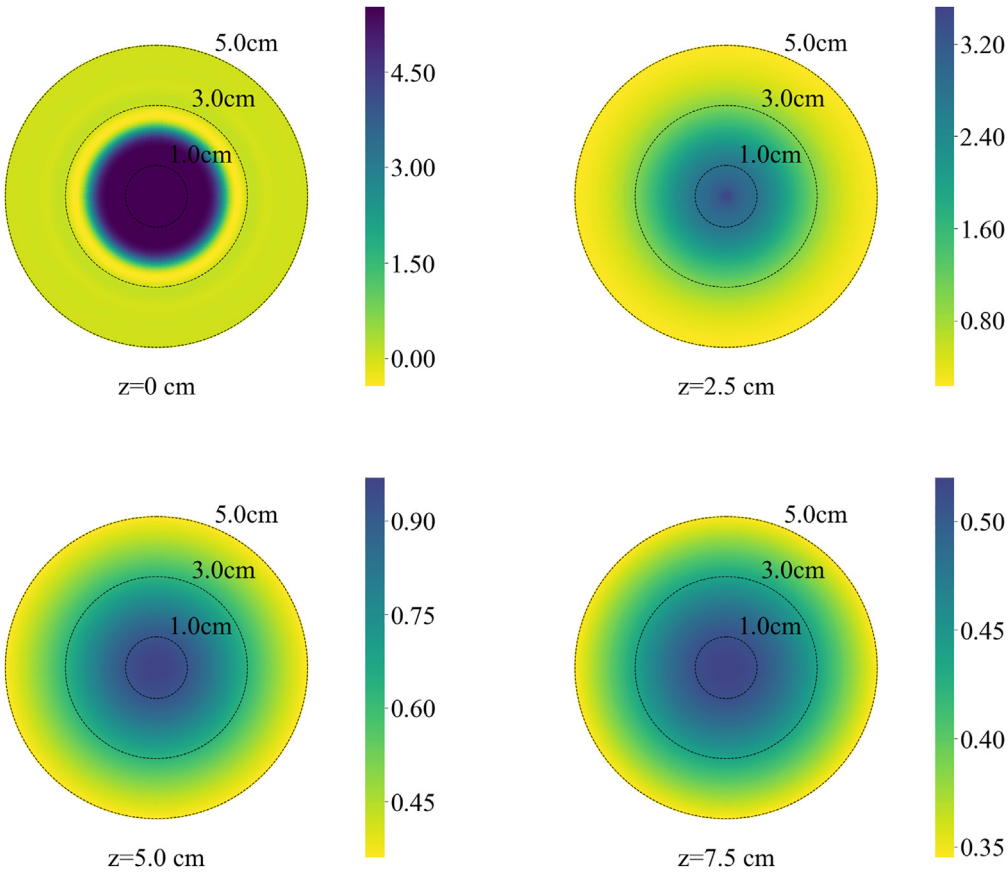

Figure 3. Analytical solutions of σ_z (P = 100 N)

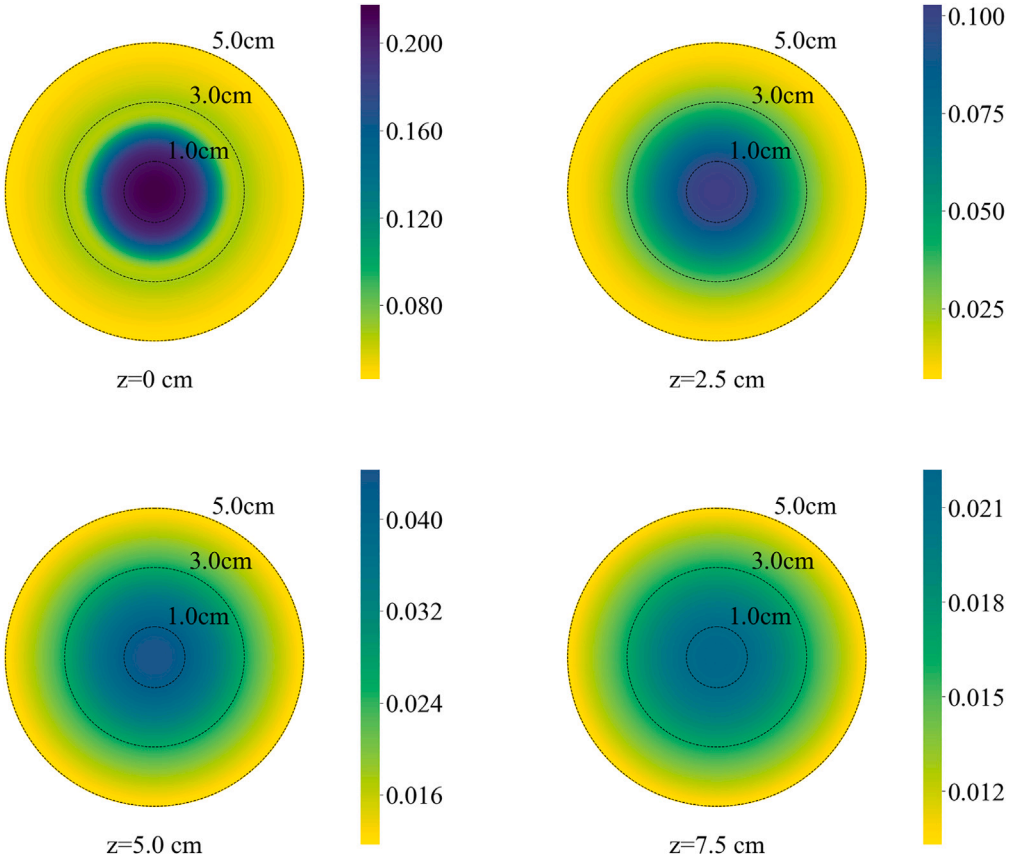

Figure 4. Analytical solutions of w (P = 100 N)

DISCUSSION

Experimental verification

In order to verify the axial stress σ_z in the proposed contact model further, a vertical contact experiment is carried out. An experimental platform is established and the vertical contact process is conducted on the platform. Meanwhile, the thin-film pressure sensor system collects the axial pressure of the contact surface and certain positions in the lunar soil simulant. The results are discussed respectively according to the position of the sensors, and are compared with the theoretical results. The results demonstrate that the theoretical analysis is reasonable and applicable to the actual situation.

Experimental platform

The experimental platform shown in Figure 6 is mainly composed of a computer with the control software, a control cabinet, a puller system, a box with lunar soil simulant, a foot model to be tested and the sensor system. When the experiment begins, the control signal is sent to the control software in the computer manually. The chip in the control cabinet accepts the signal and transforms it to the current signal to control the puller system. Then the puller system is able to move as expected and push the foot model forward. The contact information is collected by thin-film pressure sensors and then sent back to the computer.

The thin-film pressure sensors are pasted on the contact surface and certain positions in the lunar soil simulant to measure the axial stress. The axial pressure P_{sen} can be obtained from the sensors directly and the axial stress σ_{sen} is calculated as:

$$\sigma_{sen} = P_{sen}/s_{sen} \quad \text{(Equation 6)}$$

where s_{sen} is the area of a single thin-film pressure sensor. For the radius 0.25cm, s_{sen} equals to 0.196 cm^2.

Experiment results on the contact surface

When the axial stress on the contact surface is tested, the arrangement of the sensors is shown in Figure 7A. The sensor S_1 collects the axial stress in the center of the contact surface, that is to say, the position of S_1 is $r = 0$ and $z = 0$. The sensor S_2, S_3 and S_4 locates on $r = 1$ cm, $r = 2$ cm and $r = 5$ cm, respectively. The total vertical force P is controlled by the puller system with force sensor and is set as 0N, 25N, 50N, 75N, 100N, 125N and 150N, respectively.

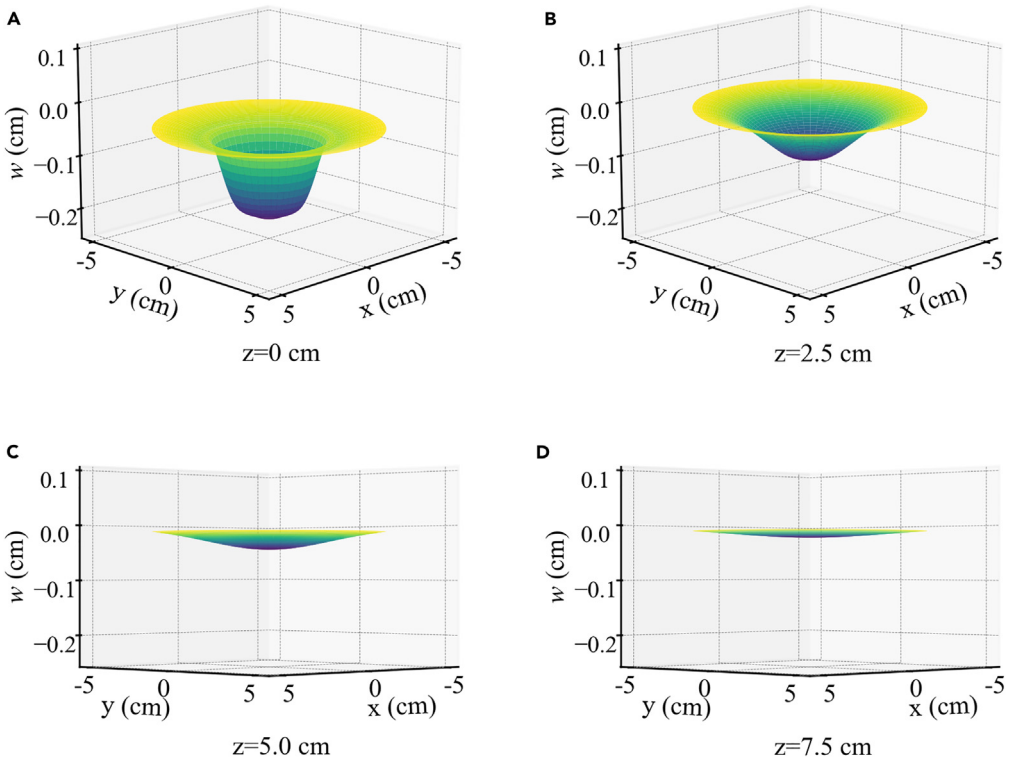

Figure 5. Analytical solutions of *w* in 3D graph (*P* = 100 N)

(A) z = 0 cm.

(B) z = 2.5 cm.

(C) z = 5.0 cm.

(D) z = 7.5 cm.

The curves are drawn according to the experimental and theoretical results and are displayed in Figure 8. The theoretical results are derived from the proposed contact model, and some of the data corresponds to the visual images of the axial stress as shown in Figure 3.

It can be seen in Figures 8A and 8B that the experimental curve fits the theoretical curve well when the total vertical force *P* is less than 125N. When *P* exceeds 125N, the slope of the theoretical curve tends to decrease and the curve no longer exhibits linear characteristic. The reason for this phenomenon is that the plastic deformation gradually dominates with the increase of *P*, while the theoretical analysis in this paper supposes that the lunar soil simulant is in elastic deformation stage. The two curves differ from each other significantly in Figure 8C. Theoretically, we want to obtain the axial stress in the certain point. However, in the experiment the sensor has an area of 0.196 cm^2, thus we can only obtain the average stress in this area. Meanwhile, sensor S_3 which is shown in Figure 8C locates at the edge of the circular plate of the bottom, thus is not attached to the contact surface completely. In other words, the suspended part of sensor S_3 reduces the average stress in this area and results in a small value.

Experiment results in the lunar soil simulant

When the axial stress in the lunar soil simulant is tested, the arrangement of the sensors is shown in Figure 7B. The total vertical force *P* is set as mentioned in subsection "Experiment results on the contact surface". The experimental results of axial stress σ_z in the lunar soil simulant are shown in Figures 9, 10, and 11 and compared with theoretical ones. The theoretical results contain the stress caused by geostatic lunar soil, and the experimental results contain the stress caused by geostatic earth soil. These parts have been subtracted in the comparison in order to see the comparative results clearly.

It can be observed in these comparative results that the theoretical curves and the experimental curves fit well in the majority of cases. For example, in the case *z* = 2.5 cm and *r* = 1 cm, the errors between the theoretical results and the experimental results are 17.11%, 4.19%, 7.17%, 3.86%, 7.48%, and 4.72% when the vertical load changes. When the axial stress is very small, such as in the case *r* = 5 cm and in the case *z* = 7.5 cm, the errors are relatively bigger. The main reason is that the sensitivity of the sensors is not high enough. The errors both on the contact surface and in the lunar soil are displayed in Figure 12. It should be noted that the data of those places with very small axial stress is not shown. The line representing 25% error is drawn in Figure 12 and it can be observed that most errors are less than 25%. Therefore, it can be considered that the errors in this experiment are controlled within a reasonable range. The curves in Figure 11 also show that the axial stress is very small both in the theoretical and experimental results. Thus, the theoretical and experimental results both

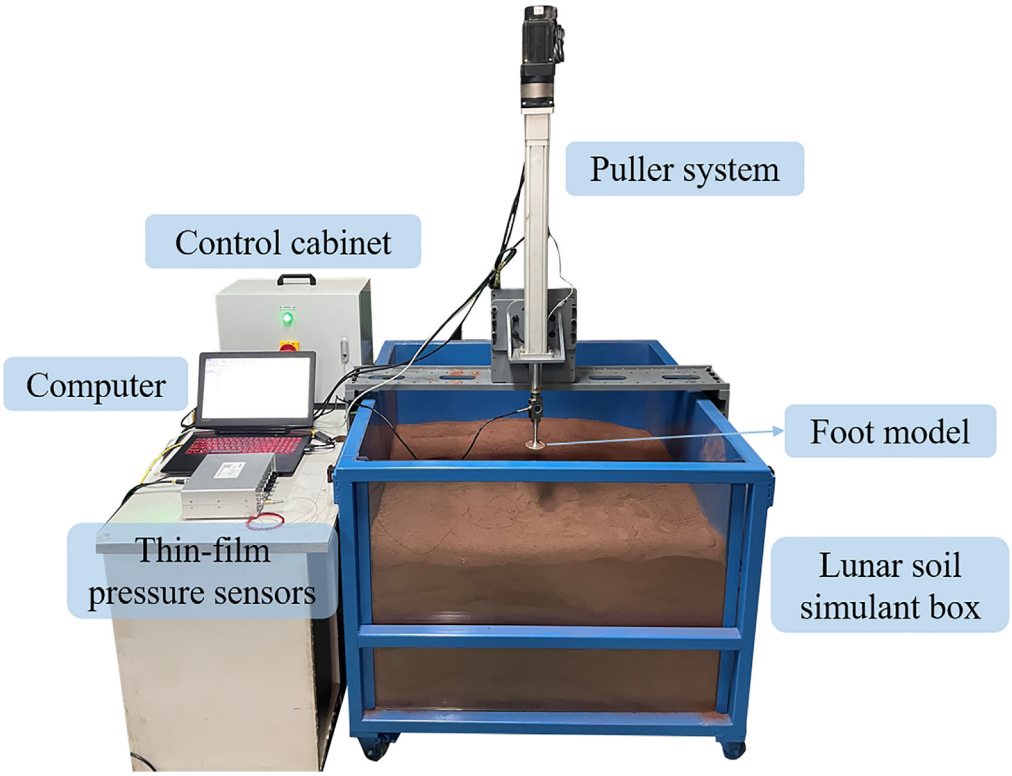

Figure 6. Experimental platform

demonstrate that the influence depth of the load is about 7.5cm, namely about three times the radius of the foot bottom. It can be concluded that the theoretical analysis is well verified by the experimental results.

Discussion on theory-experiment comparison results

It can be obtained from the comparison results which are demonstrated in the last two subsections that the curves are very close when the total vertical force *P* is less than 125N. When *P* is more than 125N, the curve which represents the experimental results tends to be flat. Meanwhile, the experimental curve no longer has the linear characteristic. The main reason is that when the vertical force *P* exceeds a

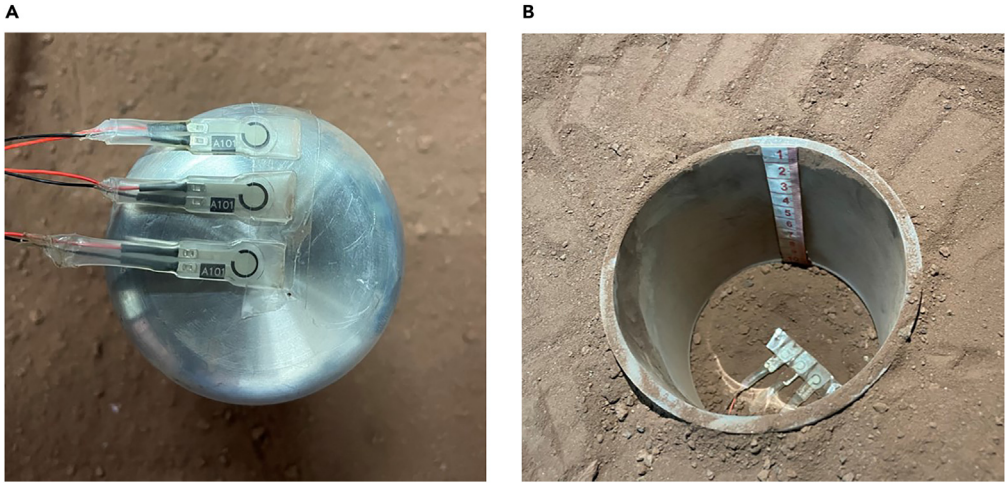

Figure 7. Arrangement of sensors

(A) Sensors on the contact surface.

(B) Sensors in the lunar soil simulant.

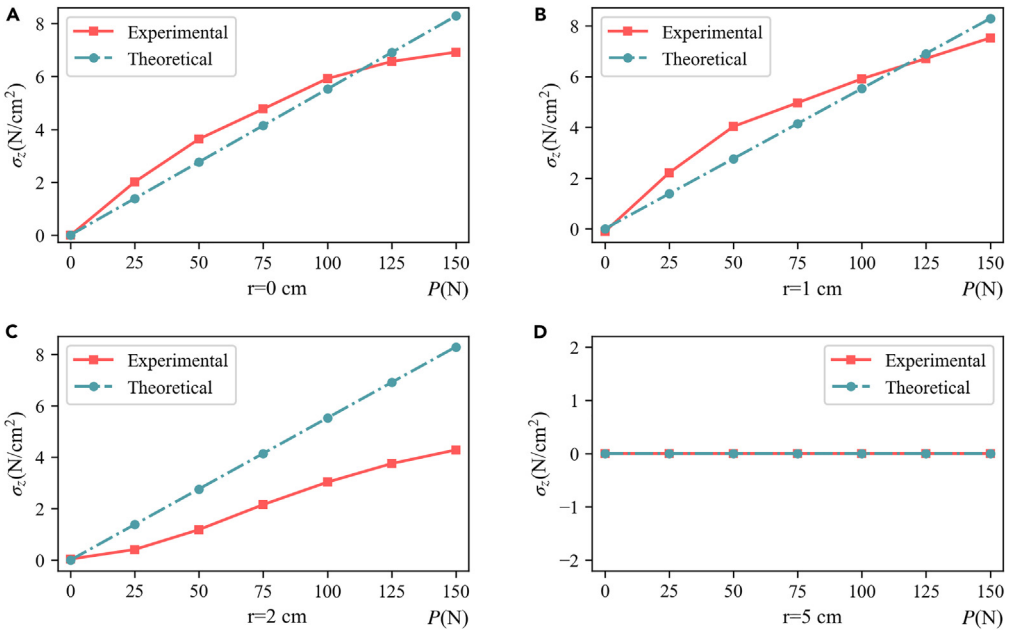

Figure 8. Axial stress σ_z on the contact surface

(A) r = 0 cm.

(B) r = 1 cm.

(D) r = 5 cm.

(C) r = 2 cm.

certain value, the lunar soil enters the elastic-plastic deformation stage. Jiang et al. (2019)[26] investigated the interface strength between the footpad and the lunar soil simulant through a loading test. The study demonstrates that strength of the interface is about 55kPa. This conclusion is consistent with the results obtained in this paper. When the vertical force *P* in our experiment is more than 125N, the axial stress on the contact surface is more than about 60kPa. In this situation, the lunar soil simulant reaches the limit of the elastic deformation stage. Then, the lunar soil simulant enters the elastic-plastic deformation stage. The stress distribution in this stage cannot be calculated precisely through the analysis proposed in this paper because the analysis is based on the assumption that the lunar soil simulant is an infinite half-elastic.

Hence, the adaptability of the analysis must be discussed. The vertical force *P* with the value of 125N can be considered as the limit of elastic stage. The shape of lunar-based equipment is shown as Figure 13 and the mass is about 12kg. When it stands on the lunar soil, the load of each foot is about 3kg. Considering the lunar gravitational acceleration is 1.63 m/s^2, the vertical load of each foot is about 4.89N and is far less than the limit of elastic stage. It can be concluded that the analysis in this paper is suitable for real application scenarios and the lunar-based equipment can still bear loads far exceeding its own weight. In other words, when the lunar-based equipment is in no-load condition or bearing loads less than 294kg on the lunar surface, the theoretical analysis in this paper is applicable and correct.

Lunar environment simulation

Although the contact model proposed in this paper is validated via terrestrial environment, the accuracy in the lunar environment is yet to be verified. The most significant characteristics of the lunar environment are the low-gravity and the high-vacuum. Generally speaking, the terrestrial gravitational acceleration is 9.80 m/s^2, while the moon has that of 1.63 m/s^2. The low gravity leads to a reduction in the self-weight stress of lunar soil, with smaller horizontal stresses. In other words, lunar soil is in a state of low confining pressure in a low-gravity environment, resulting in a slight decrease in bearing capacity. At a microscopic level, the low gravity has certain effects on the internal pores, micro-shear zones, force chains, and the evolution of the lunar soil particle aggregates. These factors contribute to the aforementioned changes. As for the high vacuum, at the microscopic level, high vacuum results in intermolecular forces between lunar soil particles, manifesting as van der Waals forces. At the macroscopic level, van der Waals forces manifest as the cohesive strength of lunar soil, slightly enhancing its overall strength.

In the past few decades, some scientists have been dedicated to experimental research on low gravity.[31–33] Existing methods include tilted table test, drop tower test, deceleration aircraft test and centrifugal force test. However, some of these methods incur significant costs (such as tower and aircraft), some of them have low accuracy (such as tower and tilted table) and some of them are not suitable for large-scale

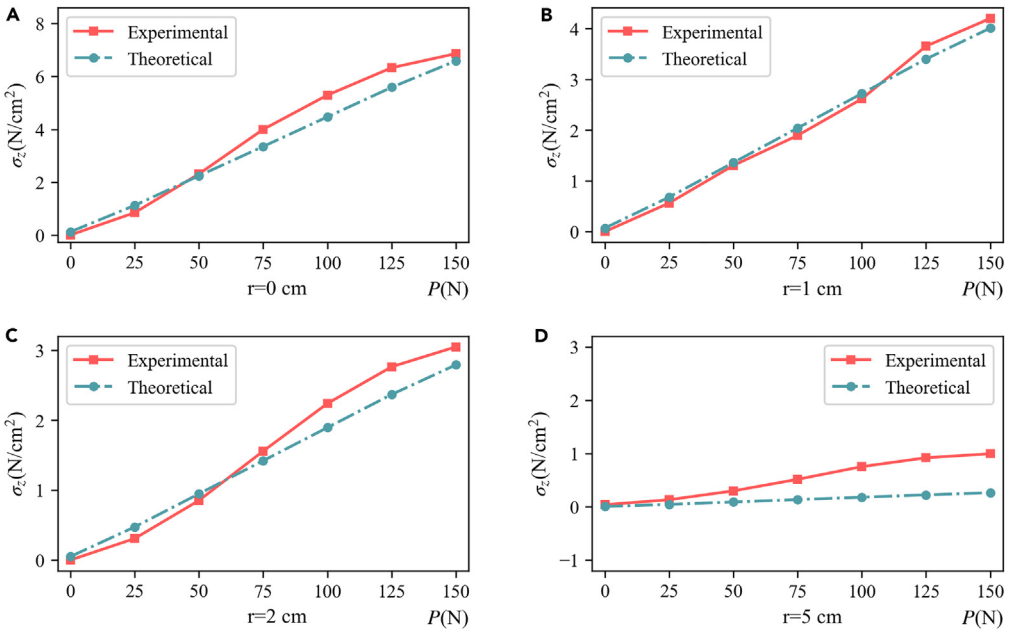

Figure 9. Axial stress σ_z on the section z = 2.5 cm

(A) r = 0 cm.

(B) r = 1 cm.

(C) r = 2 cm.

(D) r = 5 cm.

mechanical experiments (such as centrifugal force test). It can be said that currently, there is no low-gravity experimental method suitable for this experiment. The same situation occurs in the verification of high-vacuum environments, and such experiments incur significant costs.

In this paper, a discrete element simulation (DEM) is conducted to validate this issue. In the simulation, the gravity is set as same as the lunar surface, and there is no atmosphere. Hence, two main characteristics of the lunar environment are simulated at the same time and the accuracy of the proposed contact model can be estimated via the simulation results.

Simulation setup

The simulation is set up to mimic the lunar surface environment as closely as possible. The foot is modeled via SolidWorks and made of ultra-hard aluminum alloy of the 7A09 model. The discrete element model of lunar soil particles is simulated via the commercial discrete element software EDEM. Meanwhile, the physical and mechanical properties of lunar soil particles were modeled based on the values of CAS-1 simulant except for the radius. Considering the computational limitations of the computer, the lunar soil particles were modeled with the median radius of 0.5mm. This value is greater than the median particle size of the simulated lunar soil. However, the investigation by Fuglsang and Ovesen pointed out that the adverse effects of the giant particle size effect on simulation errors can be neglected, as long as the median particle size is less than 1/35th of the size of the foot.[34] The conditions of the simulation is designed as same as the visual results of the theory, namely the total pressure is p = 100N. The simulation model is shown in Figure 14.

Simulation results

The simulation result of the foot pressure is displayed in Figure 15A and there is an intuitive comparison with theoretical result of surface pressure which is shown in Figure 15B. Referring to the color bars next to the two subfigures, it can be observed that in the central region, the pressure in both subfigures is around 5.00 N/cm^2. In the edge region of the foot, namely A_2 as shown in Figure 1B, there is a noticeable decrease in pressure. In the very edge region of the A_2, the pressure drops almost to zero. In the region outside the foot, the pressure is zero. Whether in Figures 15A or 15B, the same phenomenon mentioned above can be observed. It can be considered that the simulation results align well with the theoretical outcomes. In other words, the accuracy of the proposed model in the low-gravity and high-vacuum lunar environment has been validated via simulation.

Limitations of the study

There are some assumptions regarding the contact model and its derivation proposed in this paper.

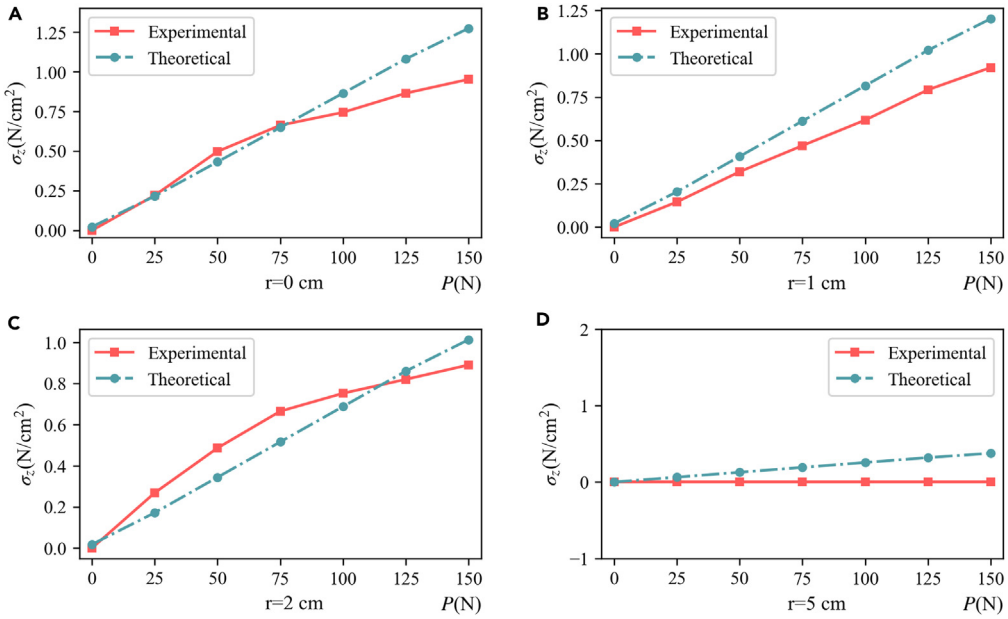

Figure 10. Axial stress σ_z on the section z = 5.0 cm

(A) r = 0 cm.
(D) r = 5 cm.
(B) r = 1 cm.
(C) r = 2 cm.

(1) First, the derivation is based on the theory of elastic mechanics. That means the lunar soil is considered as an elastic half-space.
(2) The properties of lunar soil are assumed to be uniform and isotropic.
(3) The spatial extent of lunar soil is assumed to be infinite.

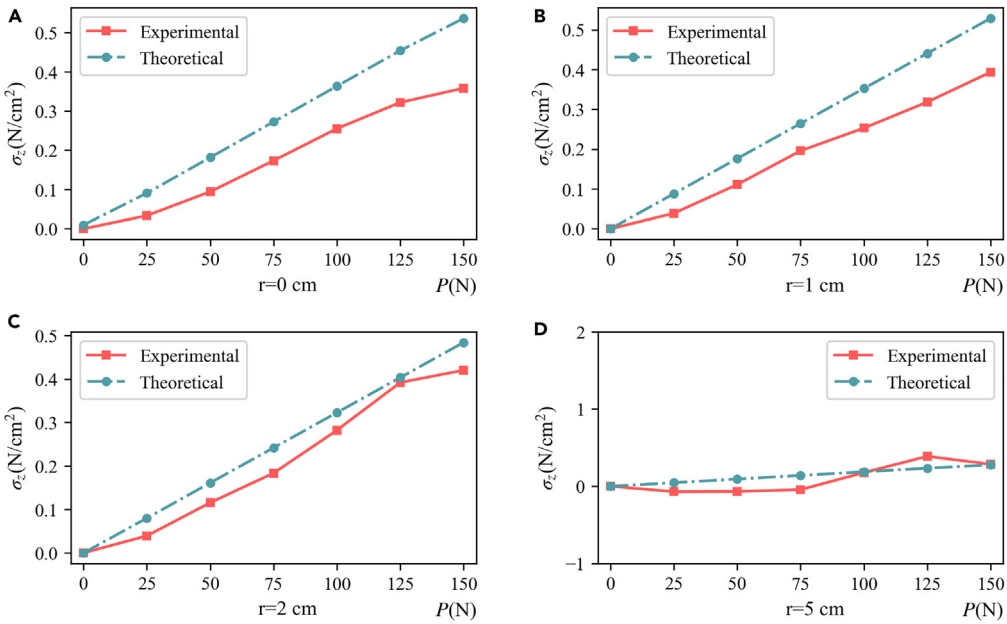

Figure 11. Axial stress σ_z on the section z = 7.5 cm

(A) r = 0 cm.
(B) r = 1 cm.
(C) r = 2 cm.
(D) r = 5 cm.

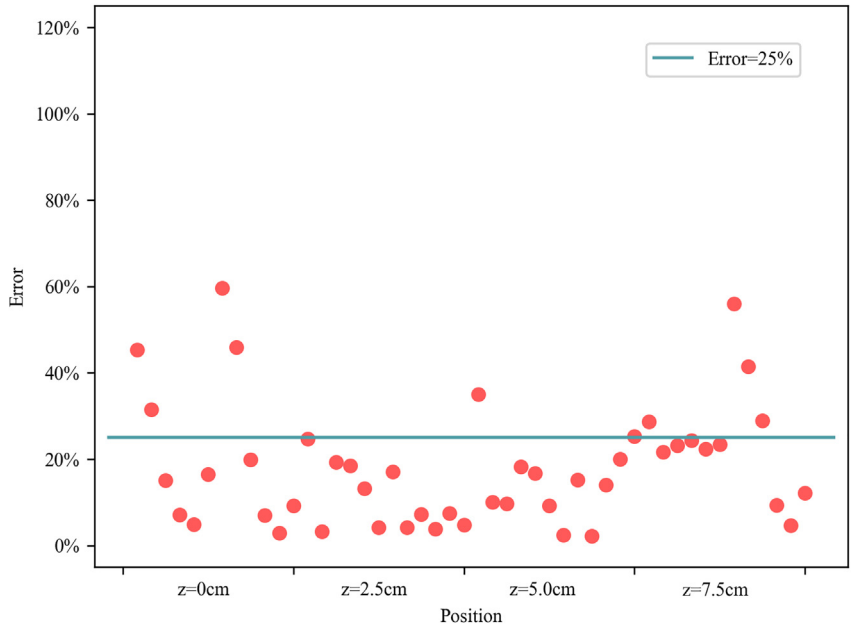

Figure 12. Errors between theoretical and experimental results

(4) Each kind of stress and displacement components are considered to be composed of three parts: one caused by the geostatic lunar soil, one caused by the circular load q_1, and one caused by the ring load q_2. They are assumed to be linearly superposable. In fact, this is based on the first assumption, namely that the derivation in this paper is within the scope of elastic mechanics.

Meanwhile, these assumptions lead to some limitations which are shown as below.

(1) In the majority of practical applications, derivations based on elastic mechanics are accurate. Although elastic deformation dominates, there is also a small amount of plastic deformation accompanying the contact process. The contact model proposed in this paper cannot separate out these plastic deformations, thus they are neglected. It should be noted that the error introduced by this handling so is small, and there is currently no method in existing literature that simultaneously considers plastic deformation.

(2) Due to the assumption that lunar soil is isotropic and infinite, the contact model proposed in this paper can only perform calculations for flat lunar soil. When the lunar soil surface has obvious undulations or craters, using the model proposed in this paper to predict stress and displacement will introduce errors. Nevertheless, the model proposed in this paper still has significant applicability and can serve as a foundation for studying lunar soil with other shapes.

STAR★METHODS

Detailed methods are provided in the online version of this paper and include the following:

- KEY RESOURCES TABLE
- RESOURCE AVAILABILITY
  - Lead contact
  - Materials availability
  - Data and code availability
- EXPERIMENTAL MODEL AND STUDY PARTICIPANT DETAILS
- METHOD DETAILS
  - Utilized CAS-1 lunar soil simulant
  - Material and shape of the foot
  - Contact mechanism analysis
- QUANTIFICATION AND STATISTICAL ANALYSIS

ACKNOWLEDGMENTS

This study was financially supported by Study on Fundamental Theories and Key Technologies in Autonomous Operation and Multi-robot Coordination of Lunar-based Equipment with Grant No. U2037602, Program of Chang Jiang Scholars of Ministry of Education, Science

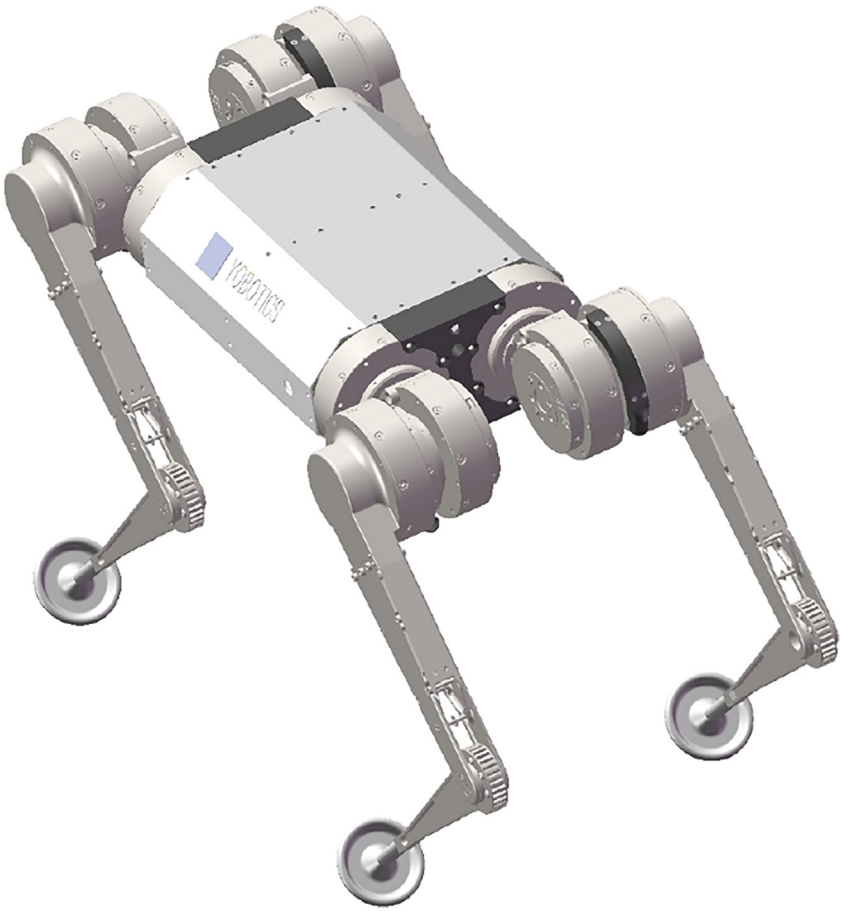

Figure 13. Lunar-based equipment

Discovery Award of Tencent Foundation and Postgraduate Research & Practice Innovation Program of Jiangsu Province with Grant No. KYCX21_0114.

AUTHOR CONTRIBUTIONS

Z.-H.C.: Original draft, data curation, formal analysis; Z.D.-X.: Conceptualization and supervision; H.F.-L.: Review and editing; D.-Y.Y.: Funding acquisition; J.-Z.Y.: Project administration; B.P.: Project administration; X.-L.Z.: Methodology of simulation; Z.-W.H.: Software. All authors reviewed the manuscript.

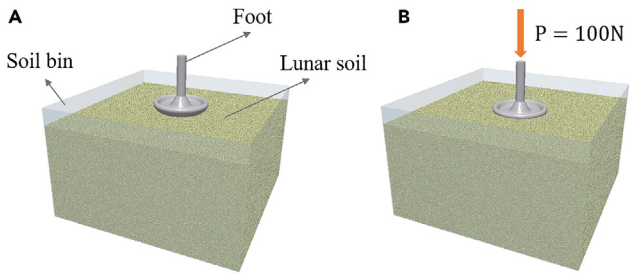

Figure 14. Simulation model
(A) Foot and lunar soil.
(B) Under loading condition.

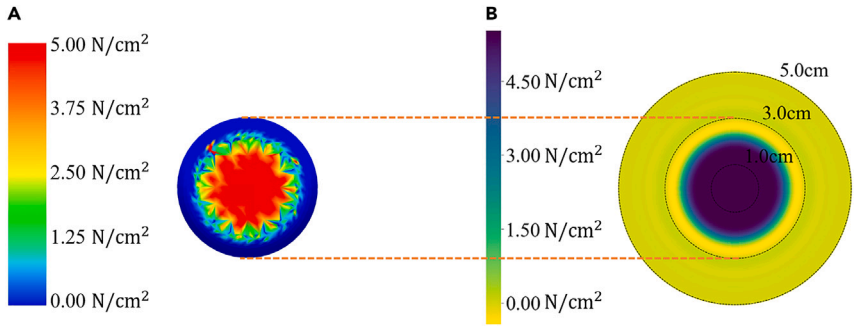

Figure 15. Simulation-theory comparison

(A) Simulation result.

(B) Theoretical result.

DECLARATION OF INTERESTS

The authors declare no competing interests.

Received: September 5, 2023
Revised: January 22, 2024
Accepted: February 20, 2024
Published: February 23, 2024

REFERENCES

1. Bender, P.L. (1994). Proposed microwave transponders for early lunar robotic landers. Adv. Space Res. *14*, 233–242. https://doi.org/10.1016/0273-1177(94)90033-7.
2. Belo, F.A.W., Birk, A., Brunskill, C., Kirchner, F., Lappas, V., Remy, C.D., Roccella, S., Rossi, C., Tikanmäki, A., and Visentin, G. (2012). The ESA Lunar Robotics Challenge: Simulating operations at the lunar south pole. J. Field Robot. *29*, 601–626. https://doi.org/10.1002/rob.20429.
3. Cohen, B.A., Chavers, D.G., and Ballard, B.W. (2012). NASA's robotic lunar lander development project. Acta Astronaut. *79*, 221–240. https://doi.org/10.1016/j.actaastro.2012.03.025.
4. Chen, Z.H., Xu, Z.D., Lu, H.F., Yu, D.Y., Yang, J.Z., Pan, B., Zhao, X.L., Hu, Z.W., and Zhen, S.C. (2023). Novel Robust Control Strategy for the Mechanical Legs of Lunar-Based Equipment. J. Aerosp. Eng. *36*, 04023061. https://doi.org/10.1061/JAEEEZ.ASENG-4988.
5. Xu, C., Xu, Z.D., Huang, X.H., Xu, Y.S., and Ge, T. (2018). Modeling and analysis of a viscoelastic micro-vibration isolation and mitigation platform for spacecraft. J. Vib. Control *24*, 4337–4352. https://doi.org/10.1177/1077546317724321.
6. Chen, G., Qiao, L., Wang, B., Richter, L., and Ji, A. (2022). Bionic Design of Multi-Toe Quadruped Robot for Planetary Surface Exploration. Machines *10*, 827. https://doi.org/10.3390/machines10100827.
7. Hauser, K., Bretl, T., Latombe, J.C., Harada, K., and Wilcox, B. (2008). Motion planning for legged robots on varied terrain. Int. J. Rob. Res. *27*, 1325–1349. https://doi.org/10.1177/0278364908098447.
8. Rohmer, E., Reina, G., and Yoshida, K. (2010). Dynamic simulation-based action planner for a reconfigurable hybrid leg–wheel planetary exploration rover. Adv. Robot. *24*, 1219–1238. https://doi.org/10.1163/016918610X501499.
9. Kolvenbach, H., Bärtschi, C., Wellhausen, L., Grandia, R., and Hutter, M. (2019). Haptic inspection of planetary soils with legged robots. IEEE Robot. Autom. Lett. *4*, 1626–1632. https://doi.org/10.1109/LRA.2019.2896732.
10. Rebula, J.R., Neuhaus, P.D., Bonnlander, B.V., Johnson, M.J., and Pratt, J.E. (2007). A controller for the littledog quadruped walking on rough terrain. In Proceedings 2007 IEEE International Conference on Robotics and Automation, pp. 1467–1473. https://doi.org/10.1109/ROBOT.2007.363191.
11. Liang, C., Gu, H., Ceccarelli, M., and Carbone, G. (2011). Design and operation of a tripod walking robot via dynamics simulation. Robotica *29*, 733–743. https://doi.org/10.1017/S0263574710000615.
12. Xu, Z.D., Chen, Z.H., Huang, X.H., Zhou, C.Y., Hu, Z.W., Yang, Q.H., and Gai, P.P. (2019). Recent advances in multi-dimensional vibration mitigation materials and devices. Front. Mater. *6*, 143. https://doi.org/10.3389/fmats.2019.00143.
13. Chen, Z.H., Xu, Z.D., Lu, H.F., Yang, J.Z., Yu, D.Y., Zhu, C., Zhen, S.C., and Zheng, H.M. (2021). A new robust control strategy for axial flux permanent magnet motor applied on legged lunar robots. J. Vib. Control *29*, 953–967. https://doi.org/10.1177/10775463211056465.
14. Chu, X., Zhang, Q., Zhou, Y., Wen, W., Li, X., and Liu, W. (2022). Locomotion Planning for Quadruped Robot Walking on Lunar Rough Terrain. Adv. Astronaut. Sci. Technol. *5*, 93–102.

Table 1. Composition of Apollo 14 sample and well-known lunar soil simulants

	SiO_2	TiO_2	Al_3O_2	MnO	FeO	MgO	CaO	Na_2O	K_2O	P_2O_5	LOI	Total
Apollo 14	48.1	1.7	17.4	10.4	0.14	9.4	10.7	0.7	0.55	0.51	–	99.6
CAS-1	49.24	1.91	15.80	11.47	0.14	8.72	7.25	3.08	1.03	0.3	0.52	99.46
JSC-1	47.71	1.59	15.02	10.79	0.18	9.01	10.42	2.7	0.82	0.66	0.11	99.01
FJS-1	49.14	1.91	16.32	13.07	0.19	3.84	9.13	2.75	1.01	0.44	0.43	98.14
MKS-1	52.59	1.01	15.91	12.28	0.22	5.41	9.36	1.9	0.58	0.14	0.5	100

Table 2. Several kinds of extra super duralumin alloy materials

Material model	Strength (MPa)	Density (g/cm^3)	Linear expansion($10^{--6\circ}$C)	Elastic modulus (GPa)	Shear modulus (GPa)
2A12	≥ 420	2.80	22.7	71	26.0
7A09	≥ 530	2.80	23.6	71	26.5
5A06	≥ 280	2.64	24.7	71	27.0

15. Wettergreen, D., Bapna, D., Maimone, M., and Thomas, G. (1999). Developing nomad for robotic exploration of the atacama desert. Rob. Auton. Syst. *26*, 127–148. https://doi.org/10.1016/s0921-8890(99)80002-5.

16. Bartsch, S., Birnschein, T., Römmermann, M., Hilljegerdes, J., Kühn, D., and Kirchner, F. (2012). Development of the six-legged walking and climbing robot SpaceClimber. J. Field Robot. *29*, 506–532. https://doi.org/10.1002/rob.21418.

17. Skonieczny, K., Delaney, M., Wettergreen, D.S., and Red Whittaker, W.L. (2014). Productive Lightweight Robotic Excavation for the Moon and Mars. J. Aerosp. Eng. *27*, 04014002. https://doi.org/10.1061/(asce)as.1943-5525.0000342.

18. Arm, P., Zenkl, R., Barton, P., Beglinger, L., Dietsche, A., Ferrazzini, L., Hamppand, E., Hinder, J., Huber, C., Schaufelberger, D., et al. (2019). Spacebok: A Dynamic Legged Robot for Space Exploration. 2019 International Conference on Robotics and Automation (ICRA) 6288-6294.

19. Yin, K., Sun, Q., Gao, F., and Zhou, S. (2022). Lunar surface soft-landing analysis of a novel six-legged mobile lander with repetitive landing capacity. Proc. Inst. Mech. Eng. Part C-J. Mech. Eng. Sci. *236*, 1214–1233. https://doi.org/10.1177/095440622199.

20. Ettouney, M.M., and Benaroya, H. (1992). Regolith mechanics, dynamics, and foundations. J. Aerosp. Eng. *5*, 214–229. https://doi.org/10.1061/(ASCE)0893-1321(1992)5:2(214).

21. Perkins, S.W. (1995). Bearing capacity of highly frictional material. ASTM Geotech. Test. J. *18*, 450–462. https://doi.org/10.1520/GTJ11020J.

22. Ding, L., Gao, H., Deng, Z., Song, J., Liu, Y., Liu, G., and Iagnemma, K. (2013). Foot–terrain interaction mechanics for legged robots: Modeling and experimental validation. Int. J. Rob. Res. *32*, 1585–1606. https://doi.org/10.1177/0278364913498122.

23. Zhai, G., Gao, P., and Meng, L. (2018). The kinematics modeling and parameter optimization of six-wheel lunar exploration robot. Int. J. Adv. Robot. Syst. *15*. https://doi.org/10.1177/1729881418770005.

24. Chen, Z.H., Xu, Z.D., Lu, H.F., Yu, D.Y., Yang, J.Z., Pan, B., Zhao, X.L., and Hu, Z.W. (2023). Novel robust control method for leg-soil system of lunar-based equipment. Int. J. Str. Stab. Dyn. 2450172. https://doi.org/10.1142/S0219455424501724.

25. Jiang, M., Xi, B., Arroyo, M., and Rodriguez-Dono, A. (2017). DEM simulation of soil-tool interaction under extraterrestrial environmental effects. J. Terramech. *71*, 1–13. https://doi.org/10.1016/j.jterra.2017.01.002.

26. Jiang, M., Xi, B., De Blasio, F.V., Lei, H., and Sun, D. (2019). Physical model tests of the bearing behavior of Tongji-1 Lunar soil simulant. J. Aerosp. Eng. *32*, 04018150. https://doi.org/10.1061/(ASCE)AS.1943-5525.0000959.

27. Kolvenbach, H., Hampp, E., Barton, P., Zenkl, R., and Hutter, M. (2019). Towards jumping locomotion for quadruped robots on the moon. In 2019 IEEE/RSJ International Conference on Intelligent Robots and Systems (IROS), pp. 5459–5466. https://doi.org/10.1109/IROS40897.2019.8967552.

28. Zhong, S., Huang, G., Qi, S., Ling, D., and Yang, J. (2013). Interface property between soft landing foot pad and simulant lunar soil. Rock Soil Mech. *4*, 1058–1062. https://doi.org/10.16285/j.rsm.2013.04.002.

29. Bui, H.H., Kobayashi, T., Fukagawa, R., and Wells, J.C. (2009). Numerical and experimental studies of gravity effect on the mechanism of lunar excavations. J. Terramech. *46*, 115–124. https://doi.org/10.1016/j.jterra.2009.02.006.

30. King, R.H., Van Susante, P., and Gefreh, M.A. (2011). Analytical models and laboratory measurements of the soil–tool interaction force to push a narrow tool through JSC-1A lunar simulant and Ottawa sand at different cutting depths. J. Terramech. *48*, 85–95. https://doi.org/10.1016/j.jterra.2010.07.003.

31. Useller, J.W. (1966). Use of Aircraft for Zero-Gravity Environment (National Aeronautics and Space Administration).

32. Weislogel, M.M. (1998). Fluid interface phenomena in a low-gravity environment: recent results from drop tower experimentation. In Space Forum, *3*Space

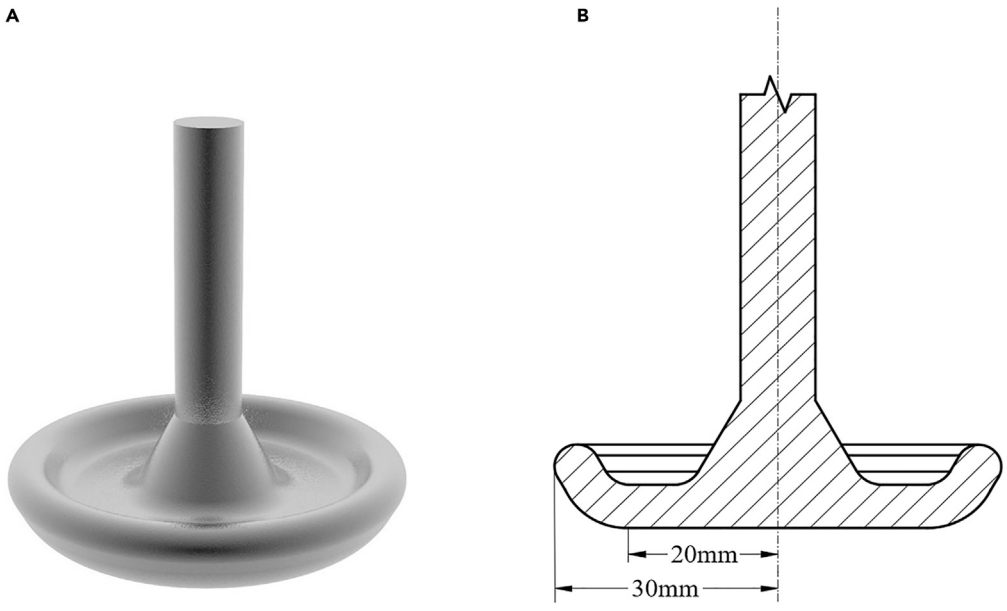

Figure 16. Shape of the foot

Forum (Gordon and Breach Science Publishers). GRC-E-DAA-TN58785.

33. Chen, J., Nie, H., Wan, J., and Lin, Q. (2014). Investigation on landing impact dynamic and low-gravity experiments for deep space lander. Sci. China. Phys. Mech. *57*, 1987–1997. https://doi.org/10.1007/s11433-014-5423-3.
34. Fuglsang, L., and Ovesen, N.K. (1988). The application of the theory of modelling to centrifuge studies. In Centrifuges in Soil Mechanics (Taylor & Francis Group), pp. 119–138.
35. Che, X., Nemchin, A., Liu, D., Long, T., Wang, C., Norman, M.D., Joy, K.H., Tartese, R., Head, J., Jolliff, B., et al. (2021). Age and composition of young basalts on the Moon, measured from samples returned by Chang'e-5. Science *374*, 887–890. https://doi.org/10.1126/science.abl7957.
36. Zheng, Y., Wang, S., Ouyang, Z., Zou, Y., Liu, J., Li, C., Li, X., and Feng, J. (2009). CAS-1 lunar soil simulant. Adv. Space Res. *43*, 448–454. https://doi.org/10.1016/j.asr.2008.07.006.
37. Willman, B.M., Boles, W.W., McKay, D.S., and Allen, C.C. (1995). Properties of lunar soil simulant JSC-1. J. Aerosp. Eng. *8*, 77–87. https://doi.org/10.1061/(ASCE)0893-1321.
38. Matsushima, T., Katagiri, J., Uesugi, K., Tsuchiyama, A., and Nakano, T. (2009). 3D shape characterization and image-based DEM simulation of the lunar soil simulant FJS-1. J. Aerosp. Eng. *22*, 15–23. https://doi.org/10.1061/(ASCE)0893-1321(2009)22:1(15).
39. Carrier, W.D., III, Olhoeft, G.R., and Mendell, W. (1991). Physical properties of the lunar surface. In Lunar Source Book, G.H. Heiken, D.T. Vaniman, and B.M. French, eds. (Cambridge University Press), pp. 475–594.
40. Reffin, M.S., Mohamad Nor, N., Rahman, N.A.A., Abdullah, N., Hatta, N., and Yahaya, M.P. (2022). Effectiveness of Large Soil Grain Sizes in Studying Impulse Characteristics of Soil. Energies *15*, 1471.

STAR★METHODS

KEY RESOURCES TABLE

REAGENT or RESOURCE	SOURCE	IDENTIFIER
Deposited data		
CAS-1 lunar soil simulant	Chinese Academy of Sciences	https://doi.org/10.1016/j.asr.2008.07.006
Parameters of CAS-1 simulant	Zheng Yongchun et al.	https://doi.org/10.1016/j.asr.2008.07.006
Extra super duralumin alloy 7A09	Chinese Academy of Sciences	ISBN: 9787515909158
Parameters of 7A09	Jian-Zhong Yang	ISBN: 9787515909158
Theoretical results	This paper	Section "results"
Original data of visual images	This paper	https://github.com/chenzhhan/Vertical-Contact
Original data of experiment	This paper	https://github.com/chenzhhan/Vertical-Contact
Software and algorithms		
MATLAB 2020b	Mathworks	https://ww2.mathworks.cn
Python 3.11	Python Software Foundation	https://www.python.org
Edem 2021	Altair	www.altair.com.cn/edem

RESOURCE AVAILABILITY

Lead contact

Further information and requests for resources should be directed to the lead contact, Zhao-Dong Xu, China-Pakistan Belt and Road Joint Laboratory on Smart Disaster Prevention of Major Infrastructures, Southeast University, Nanjing 210096, China. Email: zhdxu@163.com.

Materials availability

The source of materials is displayed in the key resources table.

Data and code availability

- Data: The dataset generated during this study is available at https://github.com/chenzhhan/Vertical-Contact.
- Code: The codes used for data analyses are available at https://github.com/chenzhhan/Vertical-Contact.
- Any additional information required to reproduce the study and reanalyze the data reported in this paper is available from the lead contact upon request.

EXPERIMENTAL MODEL AND STUDY PARTICIPANT DETAILS

The experimental model and study participant details are described in the main text (See method details section).

METHOD DETAILS

Utilized CAS-1 lunar soil simulant

Lunar soil is mainly formed by the rocks on the lunar surface. In billions of years, the impact of meteorite, cosmic rays and huge temperature differences made the rocks melt and crack constantly, and finally the lunar soil was formed. The spacecraft Chang'e 5 brought back the real lunar soil taken from the lunar surface in December 2020,[35] however, the real lunar soil is too rare to conduct so many experiments and researches. Therefore, researchers developed several types of lunar soil simulant based on the parameters of the real lunar soil and used them in the related research projects.

In this paper, CAS-1 lunar soil simulant produced by Chinese Academy of Sciences is used in the experiment. [36] For the purpose of comparison, mechanical properties of CAS-1 lunar soil simulant is also used in the analytical calculation and DEM simulation. CAS-1 simulant has two main advantages—accurate material composition and mechanical properties.

(1) CAS-1 simulant possesses material composition closest to real lunar soil. Nearly all the studies on the lunar soil simulants were carried out based on the composition analysis on the real lunar soil retrieved by Apollo 14. Thus, the composition comparison with the Apollo 14 sample is a critical index to evaluate the simulant. The following Table 1 provides a comparison between the composition of well-known simulants and the Apollo 14 sample.

Some information can be obtained from Table 1. In some major component comparisons, such as SiO_2, TiO_2 and Al_3O_2, CAS-1 simulant exhibits nearly the highest accuracy. Among them, JSC-1, FJS-1 and MKS-1 are the simulants that closely resemble real lunar soil.[37,38]

(1) CAS-1 simulant exhibits macroscopic mechanical properties similar to real lunar soil. Besides the composition, mechanical properties is also a vital factor that influences the lunar soil mechanism. Some important mechanical parameters include particle size, angle of internal friction and cohension. The median particle size of CAS-1 simulant is 85.9 μm. According to the information from Apollo spacecrafts, Apollo 11 sample has the median of 48–105 μm, Apollo 12 sample has one of 42–94 μm, Apollo 14 has one of 75–102 μm, and Apollp 15 has one of 51–108 μm.[39]. Although there is no more detailed information, it can be seen that the data of CAS-1 falls within the range. Similar situations occur in the case of angle of internal friction and cohension. For real lunar soil samples, the angle of internal friction has a range of 25–50 deg, and cohesion has a range of 0.26–1.8 kPa. CAS-1 simulant has the ones of 33.3 deg and 1.0 kPa. Due to the fact that the parameters of real lunar soil fall within a certain range, it is hard to compare the different simulants, for nearly all the aforementioned well-known simulants have the parameters falling within the corresponding range. Nevertheless, the accuracy of CAS-1 is beyond doubt. As a comparison, the cohesion of terrestrial soil is several times greater than that of lunar soil, and its angle of internal friction is much lower.

Overall, CAS-1 lunar soil simulant is a kind of out-standing simulant, and it represents the international cutting-edge level in accurately simulating lunar soil properties.

Material and shape of the foot

The foot of the lunar-based equipment is made of extra super duralumin alloy. Compared with other common metal materials, such as the iron alloy, the copper alloy and the titanium alloy, the extra super duralumin alloy has advantages of light quality and high strength. Meanwhile, the extra super duralumin alloy is not magnetic and has excellent heat resistance and corrosion resistance, thus it is not easily disturbed by the complex lunar environment. The characteristics of several kinds of aluminum alloy materials commonly used in aerospace engineering are shown in Table 2.

The extra super duralumin alloy of the model 7A09 is chosen to produce the foot for its highest strength and outstanding comprehensive performance.

As for the shape of the foot, the bottom surface of the foot is a circular plate and the edge is raised in the form of curved surface. Its conceptual graph is shown in Figure 16A and its sectional view is shown in Figure 16B.

The size of the foot is affected by two main factors. The first one is the experimental environment of the laboratory. The foot needs to be reduced in proportion to adapt to the size of the test box, sensors, and the loading equipment. On the other hand, the size of foot must be much bigger than the particle size of the lunar soil to avoid the grain-size effect.[34,40] The grain-size effect has a significant influence on the measurement in the experiment, especially the measurement of the soil stress, for the relatively large particle size makes the lunar soil cannot be regarded as an elastomer with uniform material. It is suggested that the diameter of the circular foot should be at least 35 times larger than the median particle diameter of the lunar soil. Considering the above factors, the maximum diameter of the foot is designed as 60mm and circular plate, namely the the bottom surface of the foot is designed with a diameter of 40mm.

Contact mechanism analysis

The stress, strain and displacement of the lunar soil are are composed of three parts:(a) the stress, strain and displacement caused by geostatic lunar soil; (b) those caused by load q_1; and (c) those caused by load q_2. In this section, the effect of lunar soil caused by q_1 is analyzed theoretically and the effect caused by q_2 can be seen as the difference between the two kinds of q_1 effect under specific parameters. Through the linear superposition of the three parts, the final results of stress and displacement distribution are finally obtained. In the contact mechanics analysis in this paper, the lunar soil is considered as an infinite elastic half-space. In other words, the analysis in this paper is only applicable to the elastic stage.

Stress method is applied in the analysis. Firstly, we have the differential equation of equilibrium Equation 7 and the compatibility equation Equation 8:

$$\begin{cases} \dfrac{\partial \sigma_r}{\partial r}+\dfrac{\partial \tau_{zr}}{\partial r}+\dfrac{\sigma_r-\sigma_\theta}{r}=0 \\ \dfrac{\partial \sigma_z}{\partial z}+\dfrac{\partial \tau_{zr}}{\partial r}+\dfrac{\tau_{rz}}{r}=0 \end{cases} \quad \text{(Equation 7)}$$

$$\begin{cases} \nabla^2\sigma_r-\dfrac{2}{r^2}(\sigma_r-\sigma_\theta)+\dfrac{1}{1+\mu}\dfrac{\partial^2(\sigma_r+\sigma_\theta+\sigma_z)}{\partial r^2}=0 \\ \nabla^2\sigma_\theta-\dfrac{2}{r^2}(\sigma_r-\sigma_\theta)+\dfrac{1}{1+\mu}\dfrac{1}{r}\dfrac{\partial(\sigma_r+\sigma_\theta+\sigma_z)}{\partial r}=0 \\ \nabla^2\sigma_z+\dfrac{1}{1+\mu}\dfrac{\partial^2(\sigma_r+\sigma_\theta+\sigma_z)}{\partial r^2}=0 \\ \nabla^2\tau_{rz}-\dfrac{\tau_{rz}}{r}+\dfrac{1}{1+\mu}\dfrac{\partial^2(\sigma_r+\sigma_\theta+\sigma_z)}{\partial r\partial z}=0 \end{cases} \quad \text{(Equation 8)}$$

where σ_r is the radial stress, σ_θ is the hoop stress, σ_z is the axial stress, z is the axial coordinate, $\tau_{zr} = \tau_{rz}$ is the shear stress, μ is the poisson ratio, and $\nabla^2 = \frac{\partial^2}{\partial r^2} + \frac{1}{r}\frac{\partial}{\partial r} + \frac{\partial^2}{\partial z^2}$ is the Laplacian.

Then, a stress function $\varphi(r,z)$ is proposed to simplify the solution. The relationship between the stress function $\varphi(r,z)$ and the stress components is expressed as Equation 9. Hence, the solution of the stress component is converted into the solution of stress function $\varphi(r,z)$.

$$\begin{cases} \sigma_r = \dfrac{\partial}{\partial z}\left[\mu\nabla^2\varphi - \dfrac{\partial^2\varphi}{\partial r^2}\right] \\ \sigma_\theta = \dfrac{\partial}{\partial z}\left[\mu\nabla^2\varphi - \dfrac{1}{r}\dfrac{\partial\varphi}{\partial r}\right] \\ \sigma_z = \dfrac{\partial}{\partial z}\left[(2-\mu)\nabla^2\varphi - \dfrac{\partial^2\varphi}{\partial z^2}\right] \\ \tau_{rz} = \tau_{zr} = \dfrac{\partial}{\partial r}\left[(1-\mu)\nabla^2 - \dfrac{\partial^2\varphi}{\partial z^2}\right]\cdot\varphi \end{cases} \quad \text{(Equation 9)}$$

Substituting Equation 9 into the compatibility equation Equation 8, it is obtained that the stress function $\varphi(r,z)$ is a biharmonic function. In other words, $\varphi(r,z)$ satisfies Equation 10.

$$\nabla^2\nabla^2\varphi(r,z) = 0 \quad \text{(Equation 10)}$$

The zero-order Hankel transformation of $\varphi(r,z)$ is expressed as:

$$\overline{\varphi}(\xi,z) = \int_0^\infty r\varphi(r,z)J_0(\xi r)dr \quad \text{(Equation 11)}$$

Thus, Equation 10 can be rewritten as:

$$\left(\frac{d^2}{dz^2} - \xi^2\right)^2\overline{\varphi}(\xi,z) = 0 \quad \text{(Equation 12)}$$

Then, the solution of Equation 12 can be calculated as an ordinary differential equation and expressed as:

$$\overline{\varphi}(\xi,z) = (A_\xi + B_\xi z)e^{-\xi z} + (C_\xi + D_\xi z)e^{\xi z} \quad \text{(Equation 13)}$$

where ξ is the integral variable of the zero-order Hankel transformation, A_ξ, B_ξ, C_ξ and D_ξ are the parameters determined by the boundary conditions.

Meanwhile, through inversion formula we have:

$$\varphi(\xi,z) = \int_0^\infty \xi\overline{\varphi}J_0(\xi r)dr = \int_0^\infty \xi\left[(A_\xi + B_\xi z)e^{-\xi z} + (C_\xi + D_\xi z)e^{\xi z}\right]J_0(\xi r)dr \quad \text{(Equation 14)}$$

In Equation 11, $J_0(\xi r)$ represents zero-order Bessel function. Bessel functions have the properties as:

$$\begin{cases} J_0'(\xi r) = -J_1(\xi r) \\ J_1'(\xi r) = \xi r J_0(\xi r) - \dfrac{J_1(\xi r)}{\xi r} \end{cases} \quad \text{(Equation 15)}$$

Applying the properties of Bessel functions Equation 15 and substituting Equation 14 in 9, all the stress components are calculated as:

$$\begin{cases} \sigma_r = \displaystyle\int_0^\infty \xi\left[\mu\frac{d^3\overline{\varphi}}{dz^3} + (1-\mu)\xi^2\frac{d\overline{\varphi}}{dz}\right]J_0(\xi r)d\xi - \frac{1}{r}\int_0^\infty \xi^2\frac{d\overline{\varphi}}{dz}J_1(\xi r)d\xi \\ \sigma_\theta = \mu\displaystyle\int_0^\infty \xi\left(\frac{d^3\overline{\varphi}}{dz^3} - \xi^2\frac{d\overline{\varphi}}{dz}\right)J_0(\xi r)d\xi + \frac{1}{r}\int_0^\infty \xi^2\frac{d\overline{\varphi}}{dz}J_1(\xi r)d\xi \\ \sigma_z = \displaystyle\int_0^\infty \xi\left[(1-\mu)\frac{d^3\overline{\varphi}}{dz^3} + (2-\mu)\xi^2\frac{d\overline{\varphi}}{dz}\right]J_0(\xi r)d\xi \\ \tau_{rz} = \displaystyle\int_0^\infty \xi^2\left[\xi^2(1-\mu)\overline{\varphi} + \mu\frac{d^2\overline{\varphi}}{dz^2}\right]J_1(\xi r)d\xi \end{cases} \quad \text{(Equation 16)}$$

Meanwhile, the radial displacement u and the axial displacement w can be calculated as:

$$\begin{cases} u = \dfrac{1+\mu}{E}\dfrac{\partial^2\varphi}{\partial r\partial z} = \dfrac{1+\mu}{E}\displaystyle\int_0^\infty \xi^2\frac{d\overline{\varphi}}{dz}J_1(\xi r)d\xi \\ w = \dfrac{1+\mu}{E}\left[2(1-\mu)\nabla^2 - \dfrac{\partial^2}{\partial z^2}\right] = \dfrac{1+\mu}{E}\displaystyle\int_0^\infty \xi\left[(1-2\mu)\frac{d^2\overline{\varphi}}{dz^2} - 2(1-\mu)\xi^2\overline{\varphi}\right]J_0(\xi r)d\xi \end{cases} \quad \text{(Equation 17)}$$

where E is the elastic modulus.

Substituting Equation 13, the stress components and displacement components can be rewritten as:

$$\begin{cases} \sigma_r = -\displaystyle\int_0^\infty \xi^3\left\{[\xi A_\xi - (1+2\mu-\xi z)B_\xi]e^{-\xi z} - [\xi C_\xi - (1+2\mu+\xi z)D_\xi]e^{\xi z}\right\}J_0(\xi r)d\xi + \frac{1}{r}U_\xi \\ \sigma_\theta = 2\mu\displaystyle\int_0^\infty \xi^3\left(B_\xi e^{-\xi z} + D_\xi e^{\xi z}\right)J_0(\xi r)d\xi - \frac{1}{r}U_\xi \\ \sigma_z = \displaystyle\int_0^\infty \xi^3\left\{[\xi A_\xi + (1-2\mu+\xi z)B_\xi]e^{-\xi z} - [\xi C_\xi - (1-2\mu-\xi z)D_\xi]e^{\xi z}\right\}J_0(\xi r)d\xi \\ \tau_{rz} = \displaystyle\int_0^\infty \xi^3\left\{[\xi A_\xi - (2\mu-\xi z)B_\xi]e^{-\xi z} - [\xi C_\xi + (2\mu+\xi z)D_\xi]e^{\xi z}\right\}J_1(\xi r)d\xi \\ u = -\dfrac{1+\mu}{E}U_\xi \\ w = -\dfrac{1+\mu}{E}\displaystyle\int_0^\infty \xi^2\left\{[\xi A_\xi + (2-4\mu+\xi z)B_\xi]e^{-\xi z} + [\xi C_\xi - (2-4\mu-\xi z)D_\xi]e^{\xi z}\right\}J_0(\xi r)d\xi \end{cases} \quad \text{(Equation 18)}$$

where $U_\xi = \int_0^\infty \xi^2\{[\xi A_\xi - (1-\xi z)B_\xi]e^{-\xi z} - [\xi C_\xi + (1+\xi z)D_\xi]e^{\xi z}\}J_1(\xi r)d\xi$.

In Equation 18, the parameters A_ξ, B_ξ, C_ξ and D_ξ are determined by the following boundary conditions:

$$\begin{cases} \sigma_z = -q_1, \tau_{rz} = 0 & z = 0 \\ \sigma_z = \sigma_r = \sigma_\theta = \tau_{rz} = u = w = 0 & z \to \infty \\ \sigma_z = \sigma_r = \sigma_\theta = \tau_{rz} = u = w = 0 & r \to \infty \end{cases} \quad \text{(Equation 19)}$$

Substituting Equation 19 in the stress and displacement expressions Equation 18 and considering the inversion formula, it can be obtained that:

$$\begin{cases} \xi^3 A_\xi = -2\mu\overline{q}_1(\xi) \\ \xi^2 B_\xi = -\overline{q}_1(\xi) \\ C_\xi = D_\xi = 0 \end{cases} \quad \text{(Equation 20)}$$

where $\overline{q}_1(\xi) = q_1 r_1 J_1(\xi r_1)/\xi$ is the zero-order Hankel transformation of the circular load q_1.

Applying $x = \xi r_1$ to replace the variable and substituting Equation 20 in 18, we have the solution including Bessel functions which have the form of $I = \int_0^\infty e^{-ax}J_1(x)J_m(bx)x^c dx$, as shown in Equation 21. σ_z and w are selected as representatives to describe the contact mechanism.

$$\begin{cases} \sigma_{zq_1r_1} = -q_1\displaystyle\int_0^\infty \left(1+\frac{z}{r_1}x\right)e^{-\frac{z}{r_1}x}J_1(x)J_0\left(\frac{r}{r_1}x\right)dx \\ w_{q_1r_1} = \dfrac{1+\mu}{E}q_1 r_1\displaystyle\int_0^\infty \left(2-2\mu+\frac{z}{r_1}x\right)e^{-\frac{z}{r_1}x}\frac{J_1(x)J_1\left(\frac{r}{r_1}x\right)}{x}dx \end{cases} \quad \text{(Equation 21)}$$

Thus, as long as the value of I is calculated, we will get the analytical solutions of stress and displacement components. The series expansion of $J_1(x)$ can be expressed as:

$$J_1(x) = \sum_{k=0}^{\infty}\frac{(-1)^k}{k!(k+1)!}\left(\frac{x}{2}\right)^{2k+1} \quad \text{(Equation 22)}$$

The other terms of I can be calculated as:

$$\int_0^\infty e^{-ax}J_m(bx)x^c dx = \frac{b^m\Gamma(m+c+1)}{a^{m+c+1}2^m\Gamma(m+1)}{}_2F_1\left(\frac{m+c+1}{2},\frac{m+c+2}{2};m+1;-\frac{b^2}{a^2}\right) \quad \text{(Equation 23)}$$

where $\Gamma(x)$ is Euler's integral of the second kind, and ${}_2F_1(a,b,c,z)$ is Gauss hypergeometric function. The value of these functions can be obtained from mathematics textbooks.

Hence, the analytical solution of I can be calculated as:

$$I = \sum_{k=0}^{\infty}\left[\frac{(-1)^k}{k!(k+1)!}\left(\frac{1}{2}\right)^{2k+1}\frac{b^m\Gamma(m+c+2k+2)}{a^{m+c+2k+2}2^m\Gamma(m+1)}{}_2F_1\left(\frac{m+c+2k+2}{2},\frac{m+c+2k+3}{2};m+1;-\frac{b^2}{a^2}\right)\right] \quad \text{(Equation 24)}$$

The terms which have the similar form with I in the expression of stress and displacement can be calculated according to Equation 24. The analytical solutions of the circular load q_1 with the scope of A_1 can be calculated as the product of Equations 22 and 24. The stress component σ_z can be expressed as:

$$\begin{aligned}\sigma_{zq_1r_1} = -q_1\left\{\sum_{k=0}^{\infty}\left[\frac{(-1)^k}{k!(k+1)!}\left(\frac{1}{2}\right)^{2k+1}\frac{\Gamma(2k+2)}{(z/r_1)^{2k+2}\Gamma(1)}{}_2F_1\left(k+1,k+\frac{3}{2};1;-\frac{r^2}{z^2}\right)\right]\right.\\ \left.+\sum_{k=0}^{\infty}\left[\frac{(-1)^k}{k!(k+1)!}\left(\frac{1}{2}\right)^{2k+1}\frac{\Gamma(2k+3)}{(z/r_1)^{2k+3}\Gamma(1)}{}_2F_1\left(k+\frac{3}{2},k+2;1;-\frac{r^2}{z^2}\right)\right]\right\}\end{aligned} \quad \text{(Equation 25)}$$

where

$$\begin{aligned}U_{q_1r_1} = q_1\left\{(1-2\mu)\sum_{k=0}^{\infty}\left[\frac{(-1)^k}{k!(k+1)!}\left(\frac{1}{2}\right)^{2k+1}\frac{(r/r_1)\Gamma(2k+2)}{(z/r_1)^{2k+2}\Gamma(2)}{}_2F_1\left(k+1,k+\frac{3}{2};2;-\frac{r^2}{z^2}\right)\right]\right.\\ \left.+\sum_{k=0}^{\infty}\left[\frac{(-1)^k}{k!(k+1)!}\left(\frac{1}{2}\right)^{2k+1}\frac{(r/r_1)\Gamma(2k+3)}{(z/r_1)^{2k+3}\Gamma(2)}{}_2F_1\left(k+\frac{3}{2},k+2;2;-\frac{r^2}{z^2}\right)\right]\right\}\end{aligned} \quad \text{(Equation 26)}$$

Meanwhile, the displacement component w can be expressed as:

$$\begin{aligned}w_{q_1r_1} = \frac{1+\mu}{E}q_1r_1\left\{(2-2\mu)\sum_{k=0}^{\infty}\left[\frac{(-1)^k}{k!(k+1)!}\left(\frac{1}{2}\right)^{2k+1}\frac{\Gamma(2k+2)}{(z/r_1)^{2k+2}\Gamma(1)}{}_2F_1\left(k+1,k+\frac{3}{2};1;-\frac{r^2}{z^2}\right)\right]\right.\\ \left.+\frac{z}{r_1}\sum_{k=0}^{\infty}\left[\frac{(-1)^k}{k!(k+1)!}\left(\frac{1}{2}\right)^{2k+1}\frac{\Gamma(2k+3)}{(z/r_1)^{2k+3}\Gamma(1)}{}_2F_1\left(k+\frac{3}{2},k+2;1;-\frac{r^2}{z^2}\right)\right]\right\}\end{aligned} \quad \text{(Equation 27)}$$

Equations 25 and 27 shows the stress and displacement components under the circular load q_1. As for the effect caused by the ring road q_2, it equals to the effect caused by a circular load with the radius of r_2 minus the effect caused by a circular load with the radius of r_1, and the value of these two kinds of load are both q_2. In other words, taking the axial stress as an example, the effect caused by the ring road q_2 can be calculated as:

$$\sigma_{zq_2} = \sigma_{zq_2r_2} - \sigma_{zq_2r_1} \quad \text{(Equation 28)}$$

where σ_{zq_2} is the axial stress under the ring load q_2, and $\sigma_{zq_2r_2}$ is the axial stress under the circular load q_2 with the radius of r_2 and $\sigma_{zq_2r_1}$ is the axial stress under the circular load q_2 with the radius of r_1.

Meanwhile, the other stress and displacement components can be expressed as the same form.

On the other hands, the components caused by the geostatic lunar soil can be expressed as:

$$\begin{cases}\sigma_z^0 = -\rho gz\\ w^0 = -\dfrac{(1+\mu)(1-2\mu)}{2E(1-\mu)}z^2\end{cases} \quad \text{(Equation 29)}$$

It can be considered that the stress components caused by the geostatic lunar soil exists in the initial state. However, it is not necessary to discuss the displacement caused by the geostatic lunar soil because there is no point to discuss the position of the floating lunar soil without gravity. Hence, as mentioned in the first paragraph in this section, the stress components under the vertical load of the lunar-based equipment's foot can be calculated as the sum of three parts: (a) stress caused by the geostatic lunar soil; (b) stress caused by the circular load q_1; (c) stress caused by the ring load q_2. Meanwhile, the displacement components are composed of that caused only by (b) and (c). To sum up, the final analytical solutions, namely the proposed contact model, are shown in Equation 30.

$$\begin{cases}\sigma_z = \sigma_z^0 + \sigma_{zq_1r_1} + \sigma_{zq_2r_2} - \sigma_{zq_2r_1}\\ w_r = w_{q_1r_1} + w_{q_2r_2} - w_{q_2r_1}\end{cases} \quad \text{(Equation 30)}$$

On the contact surface, namely in the case $z = 0$, the results of ${}_2F_1\left(k+1, k+\frac{3}{2}; 1; -\frac{r^2}{z^2}\right)$ in Equation 25 doesn't have a mathematical meaning. Therefore, another Bessel function expansion formula of I which is shown in Equation 31 is taken to calculate the values in the case $z = 0$.

$$\int_0^\infty J_1(x)J_0\left(\frac{r}{a}x\right)x^{-1}dx = \begin{cases} {}_2F_1\left(\frac{1}{2}, -\frac{1}{2}; 1; \frac{r^2}{r_1^2}\right) & r < r_1 \\ \frac{2}{\pi} & r = r_1 \\ \frac{a}{2r}{}_2F_1\left(\frac{1}{2}, \frac{1}{2}; 2; \frac{r^2}{r_1^2}\right) & r > r_1 \end{cases}$$

$$\int_0^\infty J_1(x)J_0\left(\frac{r}{a}x\right)dx = \begin{cases} 1 & r < r_1 \\ \frac{1}{2} & r = r_1 \\ 0 & r > r_1 \end{cases}$$

$$\int_0^\infty J_1(x)J_1\left(\frac{r}{a}x\right)dx = \begin{cases} \frac{r}{2a} & r < r_1 \\ \frac{a}{2r} & r \geq r_1 \end{cases} \quad \text{(Equation 31)}$$

Substituting Equations 31 into 18, when the load is q_1 and the area is r_1, the axial stress component on the contact surface can be expressed as:

$$\sigma_{zq_1r_1} = \begin{cases} -q_1 & r < r_1 \\ -\frac{q_1}{2} & r = r_1 \\ 0 & r > r_1 \end{cases} \quad \text{(Equation 32)}$$

Meanwhile, the displacement component w on the surface can be expressed as:

$$w_{q_1r_1} = \begin{cases} \frac{2q_1r_1(1-\mu^2)}{E}{}_2F_1\left(\frac{1}{2}, -\frac{1}{2}; 1; \frac{r^2}{r_1^2}\right) & r < r_1 \\ \frac{q_1r_1^2(1-\mu^2)}{Er}{}_2F_1\left(\frac{1}{2}, -\frac{1}{2}; 1; \frac{r_1^2}{r^2}\right) & r \geq r_1 \end{cases} \quad \text{(Equation 33)}$$

The stress and displacement components on the contact surface are also need to be integrated through Equation 30.

QUANTIFICATION AND STATISTICAL ANALYSIS

All the statistical analysis and the results are described in the main text (See results section). Data are displayed in Figures 3, 4, 5, 8, 9, 10, 11, and 12.